Nifuroxazide Activates the Parthanatos to Overcome TMPRSS2:ERG Fusion-Positive Prostate Cancer

Chengxun Li[1,2], Jiale Zhang[1], Qiming Wu[1], Anuj Kumar[1,3], Guihong Pan[1], and David J. Kelvin[1,3,4]

ABSTRACT

Fusion of the E-26 transformation-specific (ETS)-related gene (*ERG*) with transmembrane serine protease 2 (*TMPRSS2*) is a crucial step in the occurrence and progression of approximately 50% of prostate cancers. Despite significant progress in drug discovery, ERG inhibitors have yet to be approved for the clinical treatment of prostate cancer. In this study, we used computer-aided drug design (CADD)–based virtual screening to screen for potential inhibitors of ERG. *In vivo* and *in vitro* methods revealed that nifuroxazide (NFZ) inhibited the proliferation of a *TMPRSS2:ERG* fusion-positive prostate cancer cell line (VCaP) with an IC_{50} lower than that of ERG-negative prostate cancer cell lines (LNCaP, DU145, and WPMY cells). Poly [ADP-ribose] polymerase 1, the critical mediator of parthanatos, is known to bind ERG and is required for ERG-mediated transcription. NFZ blocked this interaction and overly activated PARP1, leading to cell death that was reduced by olaparib, a PARP1 inhibitor. These results show that NFZ inhibits ERG, leading to parthanatic cell death.

Introduction

According to the International Agency for Research on Cancer statistics, the mortality rate of prostate cancer among men was 6.8% worldwide, ranking fifth, whereas the incidence was 14.1%, ranking second among all cancers (1). At present, androgen deprivation therapy is an important, but largely palliative treatment for prostate cancer, and second-generation anti androgen drugs, such as abiraterone and enzalutamide, have been shown to be effective in prolonging the survival of patients with prostate cancer (2). However, about 10% to 20% of the patients develop castration-resistant prostate cancer (CRPC), most of whom lack appropriate clinical treatment, eventually leading to death (3). New studies have brought PARP inhibitors into the treatment of metastatic CRPC, but only for patients harboring *BRCA1*, *BRCA2*, or *ATM* mutations (4). Despite beneficial advances in the treatment of prostate cancer with newer therapies such as immunotherapy, patient options remain limited (5). There is an urgent need to develop new drugs for patients with prostate cancer that are safe and have a large therapeutic range.

After years of exploration, researchers have discovered multiple potential therapeutic targets for prostate cancer. In 2005, Tomlins and colleagues confirmed that transmembrane serine protease 2 (*TMPRSS2*):*ERG* fusion is very common in European and American individuals with prostate cancer (about 50%; ref. 6). The E-26 transformation-specific (ETS)-related gene (*ERG*) is an important member of the ETS family, which can be used as an activator or repressor of transcription by binding to DNA (7). After fusion with the androgen-driven promoter of *TMPRSS2*, the expression of ERG is upregulated and enhances progression of prostate cancer (6). Therefore, finding an effective ERG inhibitor can be expected to benefit the current treatment of prostate cancer.

Through high-throughput drug screening, Mohamed and colleagues used an In-Cell Western Assay with the highly specific ERG-MAb to screen small-molecule libraries for inhibition of the ERG protein and found that ERGi-USU, a small molecule inhibitor, showed a robust inhibitory effect on ERG-positive cells (8). Malhotra and colleagues recently reported the new and more potent ERG inhibitor ERGi-USU-6 developed by structure-activity studies from the parental ERGi-USU (9). YK-4–279, a small molecule inhibitor of EWS-FLI1, has also been reported to inhibit ERG- and ETV1-mediated prostate cancer (10). However, these small molecules mentioned above are still far from clinical application because their safety and efficacy remain unknown (11). Nifuroxazide (NFZ) is a nitrofuran drug. Its safety has been recognized clinically, and it is chiefly used to treat acute infectious diarrhea (12). In this study, we identified NFZ as an effective TMPRSS:ERG inhibitor and showed that NFZ activates parthanatos in *TMPRSS2:ERG*-positive prostate cancer cells, which is a new mode of action and different from the ERG inhibitors mentioned above.

Materials and Methods

Virtual screening and molecular docking simulation

To screen the inhibitors of ERG, we performed virtual screening using drug structures in the DrugBank repository 5.1 (13). The solved 3D structure of the ETS domain of ERG complexed to DNA (PDBID: 4IRI) was attained from the RCSB-Protein Data Bank (PDB) for molecular docking (14). LeDock (http://lephar.com), a fast and accurate flexible docking software, was used to screen for small molecules against the ETS domain of ERG (15). The docking site was defined as amino acids SER349-TYR356.

All selected molecules were converted from SDF to PDBQT format with the aid of Open Babel software (16). Polar hydrogens and Gasteiger charges were added to each molecule using Autodock toolkit (17). The solved 3D structure of the ETS domain of ERG complexed to DNA (PDBID: 4IRI) was attained from the RCSB-PDB (18). Before docking, the ERG protein structure was prepared

[1]Laboratory of Immunity, Shantou University Medical College, Guangdong, China. [2]Institutes of Biomedical Sciences, Fudan University, Shanghai, China. [3]Department of Microbiology and Immunology, Faculty of Medicine, Canadian Center for Vaccinology, Dalhousie University, Halifax, NS, Canada. [4]Guangdong Provincial Key Laboratory of Infectious Diseases and Molecular Immunopathology, Shantou University Medical College, Guangdong, China.

Corresponding Author: David J. Kelvin, Laboratory of Immunity, Shantou University Medical College, Guangdong, China. E-mail: David.kelvin@dal.ca

Mol Cancer Ther 2023;22:306–16

doi: 10.1158/1535-7163.MCT-22-0159

with different structural changes including the removal of water and heteroatoms, the addition of polar hydrogen, and Kollman charges using different modules available in an Autodock toolkit (17). Before docking, eight residues namely, Ser349, Arg350, Ala351, Leu352, Arg353, Tyr354, Tyr355, and Tyr356 were defined as pocket site residues based on the previous report (18). The Lammarckian GA 4.2 algorithm was used for virtual docking, and other parameters were set by default (19). Visual analysis was carried out by Discovery studio visualizers.

Cell lines

Prostate cancer cell lines (PC3, VCaP, WPMY, LNCaP, DU145) were kindly provided by the stem cell bank of the Chinese Academy of Sciences. All cell lines were identified by short-tandem repeat and tested by PCR for *Mycoplasma* before the *in vitro* experiment in September 2019. *In vitro* experiments were completed within 30 passages of cell. RPMI1640 medium (Gibco, USA) and DMEM high glucose medium (Gibco, USA) were supplemented with 1% antibiotic, 100x antimycotics (Gibco, USA), and 10% special-grade South American FBS (Thermo Fisher Scientific, USA). DMEM high glucose medium was used to culture PC3, VCaP, and DU145, while RPMI1640 medium was used for WPMY and LNCaP cells. Cells were incubated at 37°C and 5% of CO_2. Because WPMY, VCaP, and LNCaP are androgen-driven cell lines, their culture medium was supplemented with 10 nmol/L R1881 (MCE, USA), a synthetic androgen.

Measurement of cell proliferation

Two thousand cells per well were seeded in a 96-well plate. After the cells adhered to the plate, the different concentrations of drugs (zidovudine, andrographolide, amoxicillin, cefixime, sulfasalazine, nifuratel, NFZ, nifursol, napabucasin, olaparib, and disulfiram purchased from MCE;nifurtimox provided by TargetMol) diluted in culture medium were added, with DMSO (Biotopped Amresco) as control. The cells were cultured at 37°C and 5% CO_2 for 72 hours. Then, 10 μL of CCK8 (MCE, USA) solution and 90 μL of corresponding medium were added into each well, and cells were incubated for an additional 2 hours, followed by measuring the absorbance at 450 nm using a FilterMax F5 filter microplate reader.

Determination of cell necrosis and apoptosis

The cells were stained with propidium iodide (PI) and Hoechst 33342 by using a Cell Necrosis and Apoptosis Assay kit (Beyotime-c1056). A BD Accuri C6 flow cytometer was used to detect fluorescence and light scattering.

Cell-cycle determination

The cells were stained with the cell-cycle detection kit (4A Biotechnology). BD Accuri C6 flow cytometry was used to detect fluorescence and light scattering.

RNA extraction

RNA extraction was completed according to the operation instructions provided by the Cell Total RNA Extraction kit (TaKaRa MiniBEST Universal RNA Extraction Kit No. 9767).

RNA sequencing analysis

Cells were treated with 1 μmol/L NFZ for 12 hours and 24 hours, respectively. Then, total RNA was extracted, and the quality of RNA was detected by agarose gel electrophoresis and Agilent 2100. Then, the sequencing was completed on a Hiseq-PE150 sequencing platform (Novogene).

FastQC and Trimmomatic were used for quality control and data filtering of FastQ files, respectively (20, 21). STAR was used for sequence alignment (22). Reference genome hg38 (grch38. P12) and gene annotation GTF (grch38, version 30, Ensembl 96) were downloaded from GENCODE (www.gencodegenes.org). RSEM was used to determine the relative levels of gene expression (23). The aforementioned software packages were run on the Ubuntu 14.04.6 system. Expected counts as the input variables were homogenized using the OmicShare platform (https://www.omicshare.com/), including the calculation counts per million and the differences of gene expression between the control groups and NFZ groups. The differentially expressed genes were screened with $|\log_2 fc| \geq 1$ and $Q < 0.05$ as the criteria, and then KEGG enrichment analysis and visualization analysis were performed. The data from this study were deposited in NCBI Sequence Read Archive under accession SRA: PRJNA913655.

RT-qPCR

Cells were treated with 2 μmol/L and 5 μmol/L NFZ, respectively, for 12 hours and 24 hours with DMSO as the control. Total RNA was extracted and reverse transcribed using PrimeScript RT Master Mix (Takara No. rr036a). The reaction solution was put into a Mastercycler nexus X1 PCR instrument, and the program was set at 37°C for 15 minutes and 85°C for 5 seconds. Real-time fluorescence quantitative PCR was performed with a TB Green Premix Ex Taq II kit (Takara No. RR820A). Primer synthesis was completed by Sangon Biotech, and the detailed information is shown in Supplementary Table S1S. PCR was performed using an ABI QS5 Real-time PCR System, following the standard procedure of two-step PCR amplification with *TUBA1C* as the reference gene.

Immunocytochemistry

Cells were fixed with 4% paraformaldehyde, permeabilized in 0.2% Triton X-100, and blocked with 3% BSA-PBS. The cells were incubated overnight at 4°C with primary antibodies against cleaved PARP1 (Beyotime, AF1567), AIF (Solarbio, K000163M), or phospho-histone H2A.X (Beyotime, AF1201). DAPI was used to stain the nucleus. Goat anti-rabbit IgG H&L Alexa Fluor 680 (Abcam, ab175773) and goat anti-mouse IgG H&L Alexa Fluor 488 (Abcam, ab150113) were used for secondary antibodies, and immunofluorescence was observed with a Zeiss LSM800 confocal laser microscope.

Western blot

The cells were collected with a scraper and lysed with RIPA lysis buffer (Beyotime, P0013) containing 1% PMSF (Beyotime, ST506). After heating with the proper amount of sample loading buffer (Invitrogen, LC2570), the mixture was separated by SDS-PAGE and transferred to a polyvinylidene difluoride membrane. No-Stain Protein Labeling Reagent (Thermo Fisher Scientific, a44449) was used to label the total protein, and fluorescent blocking buffer (Thermo Fisher Scientific, 37565) was used for blocking membranes. Membranes were incubated with primary antibodies, for ERG (Beyotime, AF1297), STAT3 (Proteintech, 60199–1-Ig), ALDH1 (Invitrogen, MA5–29023), PARP1 (Proteintech, 66520–1-Ig), cleaved PARP1 (Beyotime, AF1567), AIF (Solarbio, K000163M), or phospho-histone H2A.X (Beyotime, AF1201), at 37°C for 1.5 hours. After washing, membranes were incubated with secondary goat anti-rabbit IgG H&L Alexa Fluor 680 (Abcam, ab175773) and goat anti-Mouse IgG H&L Alexa Fluor Plus 800 (Life Technologies, A32730), and protein bands were visualized using a Bio-Rad ChemiDoc MP fluorescence imaging system or Amersham Typhoon5. Image lab 5.2 software was used to quantify and normalize the proteins (24).

Construction of ERG-overexpressing DU145 cells and PARP1-overexpressing VCaP cells

pCDH-ECMV-3*Flag-ERG-EF1a-Puro (FENGHUISHENGWU, *ERG* gene ID: NM_182918) is a lentiviral ERG expression vector expressing a C-terminal FLAG tag. And pCDH-ECMV-6*His-PARP1-EF1a-Puro (FENGHUISHENGWU, *PARP1* gene ID: NM_001618) is a lentiviral PARP1 expression vector, which expresses a C-terminal 6*His tag. With the empty vector as the control, the plasmids (empty vector, ERG or PARP1 expression vector), pCMV-VSV-G (Beyotime, D8215) and pCAG-dR8.9 (Beyotime, D8216) were cotransfected into 293T cells to generate lentivirus. After virus enrichment, DU145 and VCaP cells were transfected with the ERG and PARP1 expression lentivirus, respectively. Stable overexpressing cell lines were selected in puromycin.

Coimmunoprecipitation

With DMSO as a control, cells were treated with 0.25 μmol/L, 0.5 μmol/L, and 1 μmol/L NFZ for 2 hours. The cells were collected with a scraper and lysed with RIPA lysis buffer (Beyotime, P0013) containing 1% PMSF (Beyotime, ST506). Lysates were divided into different groups. For ERG-immunoprecipitation experiments, ERG was used as the bait protein and PARP1 was the target protein. The ERG was precipitated with anti-flag magnetic beads (Beyotime, P2115) and was detected by Western blotting. For PARP1-immunoprecipitation experiments, PARP1 was used as the bait protein and ERG was the target protein. The PARP1 was precipitated with PARP1 monoclonal antibody (Proteintech, 66520–1-Ig) according to the instructions of an immunoprecipitation kit (Proteintech, PK10007) and anti-6*His magnetic beads (Beyotime, P9811).

Surface plasmon resonance

ERG (Cusabio, csb-yp007781hu), STAT3 (Proteintech, ag0360), and ALDH1 (Proteintech, ag8551) were fixed on Series Sensor Chip CM5 (BR-1005–30, GE) and were analyzed with a Biacore 8K system (GE Healthcare Life Sciences, GE).

Animal studies and models

Xenograft tumors were established by injecting 4×10^6 VCaP cells subcutaneously on the left abdomen of male SCID mice, obtained from Charles River Laboratories. When tumors reached ∼100 mm^3, the mice were randomly assigned to treatment and control groups, six mice per group. The treatment groups were injected intraperitoneally (i.p.) with 75 mg/kg once a day or gavage administration with 37.5 mg/kg twice a day, while the control group was injected i.p. with the corresponding solvent. Data were collected every 3 days. The values of alanine aminotransferase (ALT) and aspartate aminotransferase (AST) in plasma were detected every 7 days by the following kits: Nanjing Jiancheng, C009–2-1; Nanjing Jiancheng, C010–2-1. When the tumor volume exceeded 2 cm^3, the experimental endpoint was reached. After the mice were euthanized, the tumors were removed for analysis. The above animal experiments were approved by Institutional Animal Care and Use Committee of SAFE (Shenzhen) Non-clinical Laboratories.

Statistical analysis

All data are presented in the form of mean ± SD unless otherwise specified. In addition to special instructions, the analysis of differences between groups was performed with GraphPad prism 8.0 for one-way ANOVA. $P < 0.05$ was considered a statistically significant difference.

Data availability statement

The data generated in this study are available within the article and its Supplementary Data files.

Results

Acquisition of the active drug

To ensure that the active drugs had clinical applicability, we used the marketed and experimental drugs included in DrugBank as the ligand library to dock with the ETS domain of ERG (13). The main parameters of docking software are binding energy and binding efficiency (Supplementary Table 2S). The better docking effect is manifested in a lower binding energy and higher binding efficiency. We not only based our results on virtual docking, but also compared with existing ERG inhibitors (8, 10), to select for compounds with substantial cell proliferation inhibition. We chose the *TMPRSS2:ERG*-positive prostate cancer cell line (VCaP) as the main model (25).

As shown in Supplementary Table 2S, nifuratel shows better docking parameters than that of other candidates, along with an acceptable inhibitory effect on VCaP (IC_{50}, 13.9 ± 1.12 μmol/L). It demonstrates that the structure of nifuratel should be the active structure, so we focus on nitrofurans. To further figure out the structure-activity relationship, we examined the inhibition of three other nitrofurans (NFZ, nifursol, and nifurtimox) on androgen-sensitive cell lines (VCaP and LNCaP; refs. 25, 26) and androgen-insensitive cell lines (PC3 and DU145), as well as the normal prostate cell line (WPMY; refs. 27–29). To evaluate the binding ability of nitrofurans to ERG, we calculated their binding energies by molecular docking simulation. The results showed that NFZ exhibited lower binding energy compared with nifuratel and nifurtimox (**Table 1**). For nifursol, the modification of two nitro groups on the benzene ring produces more hydrogen bond interactions with the receptor, resulting in a binding energy lower than that of NFZ (Supplementary Fig. S1). In the cell proliferation inhibition assay, NFZ shows better IC_{50} of VCaP cells than that of the other nitrofurans (**Table 1**). So, the low activity of nifursol indicates that the modifications at the benzene ring are limited to the para position, whereas modifications at other sites may reduce the efficacy.

However, NFZ has been characterized to target STAT3 and inactivate ALDH1 to inhibit multiple myeloma and melanoma cells, respectively (30, 31). Therefore, we chose the STAT3 inhibitor (napabucasin) and ALDH1 inhibitor (disulfiam) to determine their ability to inhibit growth of different cell lines under the same conditions (32, 33). Expression of the target proteins in five cell lines was determined by Western blotting (**Fig. 1A** and **B**; Supplementary Fig. S2). For this, we adopted multiple fluorescence detection and total protein normalization to measure the protein levels (34). Napabucasin has a stronger inhibitory effect on DU145 (IC_{50}, 0.16 ± 0.05 μmol/L) than the other four cell lines (**Table 1**), which is consistent with the expression level of STAT3. VCaP has higher levels of ERG and ALDH1 compared with the other cell lines, which indicates NFZ may play an inhibitory role through ERG or ALDH1. However, disulfiram has no obvious inhibitory effect on VCaP cells (IC_{50} > 30 μmol/L). The lower IC_{50} value of NFZ on VCaP (2.65 ± 0.08 μmol/L) suggests that ERG is the target for NFZ, hereinafter referred to as NFZ, in VCaP cells.

NFZ targets ERG and inhibits its function

To verify whether NFZ could bind to ERG, we adopted surface plasmon resonance (SPR) to obtain the kinetic characteristics and affinity constant (K_D) of NFZ and ERG (**Fig. 1C**). The lower the K_D value is, the stronger the affinity between the two molecules will be. And the rapid rise and fall of the curves indicates that NFZ and ERG

Table 1. Growth inhibitory IC_{50} and binding energy of NFZ in five different cell lines.

Compound	VCaP	PC3	LNCaP	DU145	WPMY	Binding energy (kcal/mol)
Nifuratel	13.9 ± 1.12	3.87 ± 0.35	>30	27.7 ± 1.11	26.6 ± 0.13	−5.4
Nifuroxazide (NFZ)	2.56 ± 0.08	3.62 ± 0.51	13.4±2.66	5.12 ± 0.63	4.53 ± 0.12	−5.9
Nifursol	>30	>30	>30	>30	>30	−6.1
Nifurtimox	>30	>30	>30	>30	>30	−5.5
Napabucasin	0.23 ± 0.05	0.29 ± 0.07	0.23 ± 0.08	0.16 ± 0.05	0.25 ± 0.01	—
Disulfiram	>30	27.0 ± 2.00	33.0 ± 3.11	22.6 ± 2.93	23.3 ± 0.49	—

Note: IC_{50}, the half maximal inhibitory concentration (μmol/L); IC_{50} values were obtained from GraphPad Prism 8.0 and shown as mean ± SD ($n = 3$ independent experiments).

were fast binding and fast dissociation, with a K_D of 10.8 μmol/L, which was obtained by fitting the saturation curve with the concentrations as the abscissa and the steady-state response as the ordinate (**Fig. 1C** and **D**). Under the same conditions, the K_D values of NFZ with STAT3 and ALDH1 were 22.8 μmol/L and 22.2 μmol/L, respectively, and the binding patterns were also "fast binding/fast dissociation" (Supplementary Fig. S3). Thus, the affinity of NFZ and ERG is twice as strong as the STAT3 or ALDH1, and they have the same binding and dissociation characteristics. Specially, we deducted the influence not only of reference channel, but also of solvent on target protein and channel (**Fig. 1C**). The subsequent signal fluctuated from low to high after the signal value of the solvent was deducted (35, 36). Moreover, RT-qPCR was used to measure the expression of genes (*PLAU*, *SERPINE1*, *SOX9*, and *LAMC2*) downstream of ERG (37). The mRNA expressions of *PLAU*, *SERPINE1*, *SOX9*, and *LAMC2* decreased with the increasing NFZ concentrations at different times (**Fig. 1E**). These results show ERG-mediated transcription is inhibited by NFZ. The results of RNA sequencing (RNA-seq) also confirmed the downregulation of the above genes (Supplementary Table).

RNA-seq analysis of NFZ acting on VCaP cells

We extracted the mRNA of VCaP cells treated with NFZ and analyzed the effect of NFZ on gene expression by RNA-seq. At 24 hours, NFZ-treated cells showed a large number of differences in gene expression compared with that of the control group (Supplementary Fig. S4) and are mainly associated with cell cycle, cytokine expression, MAPK signaling pathway and DNA damage repair, based on KEGG enrichment analysis (**Fig. 2A** and **B**; Supplementary Fig. S4). We verified the stability of 12 (92%) of the 13 differentially expressed genes by RT-qPCR (**Fig. 1E**; Supplementary Fig. S5).

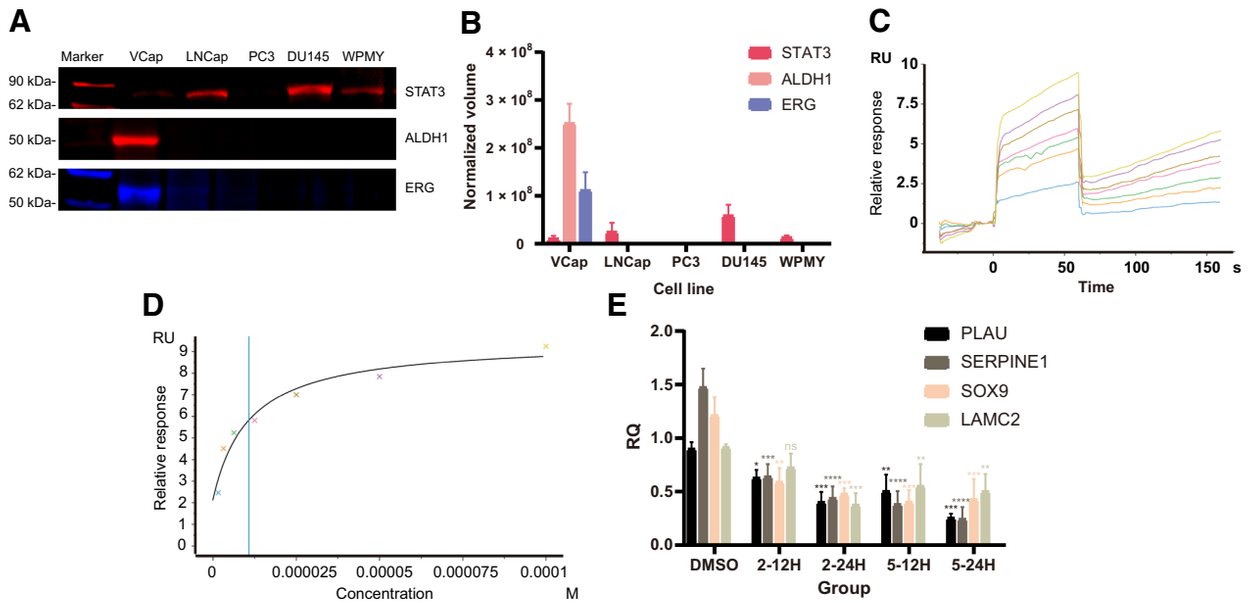

Figure 1.

NFZ targets the ETS domain of ERG. **A,** ERG, ALDH1, and STAT3 Western blots. Samples are untreated lysates from five different cell lines. Uncropped blots are shown in Supplementary Fig. S2. **B,** The quantification of ERG, ALDH1, and STAT3 was normalized to total protein and analyzed with Image Lab 5.2 software using the first sample as a reference. **C,** ERG and NFZ affinity determination curve. NFZ concentrations decrease from top to bottom. **D,** The fitted curve of the affinity. **E,** Expression of genes downstream of ERG, determined by RT-qPCR. RQ, relative quantification. DMSO was used as a control. The abscissa indicates 2 or 5 μmol/L NFZ treatment for 12 or 24 hours. Results are shown as mean ± SD ($n = 3$ independent experiments; ns, not significant; *, $P < 0.05$; **, $P < 0.01$; ***, $P < 0.001$; ****, $P < 0.0001$), compared with the DMSO control, by Dunnett multiple comparisons test.

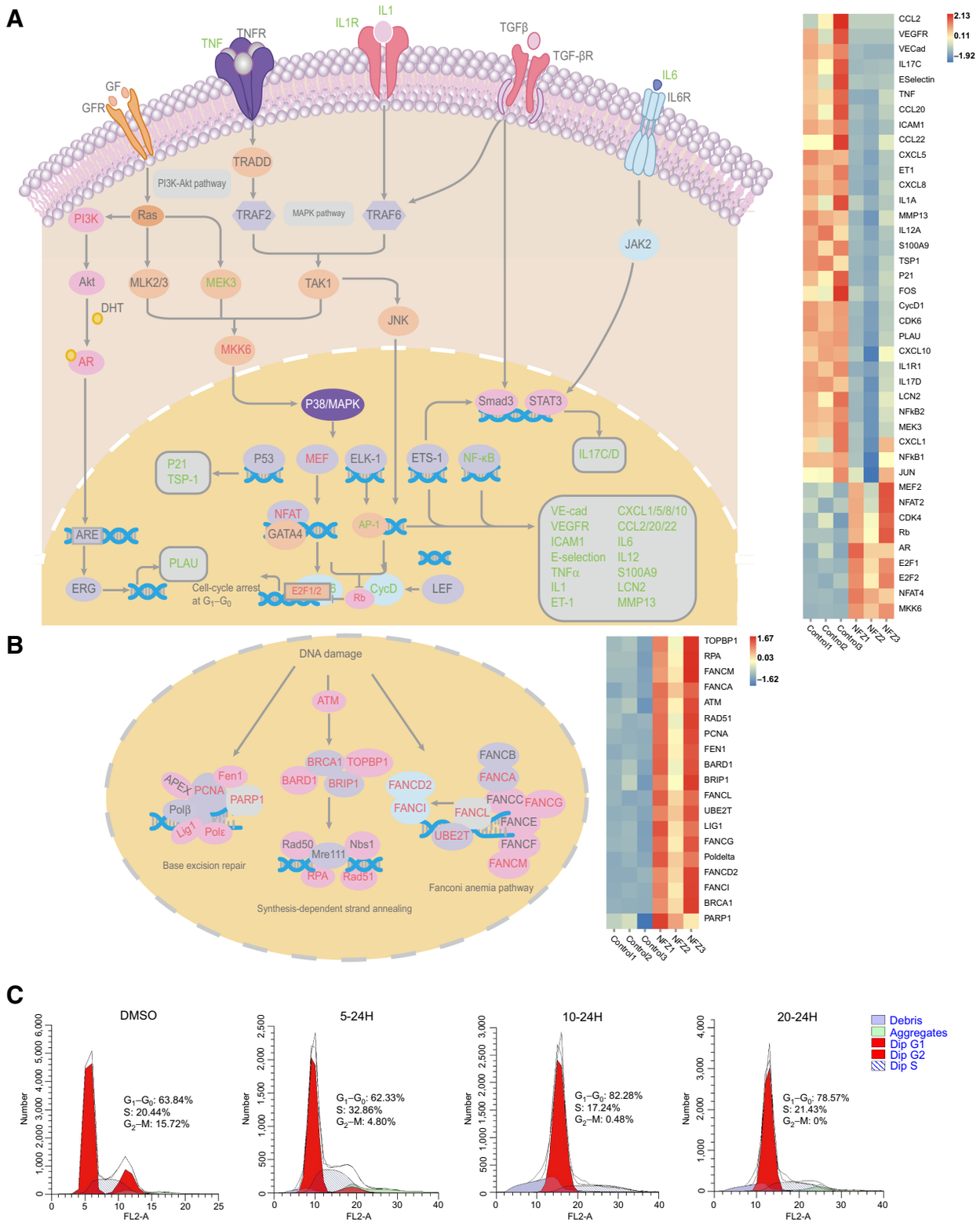

Figure 2.

RNA-seq analysis of VCaP cells treated with NFZ. **A,** Differential gene enrichment map. On the left is a pathway enrichment map of differential genes. Red font represents upregulation, while green represents downregulation. On the right is a heatmap of the differential gene expression between untreated and NFZ-treated VCaP cells. Results are shown as three independently repeated groups. NFZ groups were treated with 1 μmol/L NFZ for 24 hours. **B,** Influence of NFZ on DNA repair pathway. **C,** Effect of NFZ on the cell cycle. VCaP cells were treated with 5, 10, or 20 μmol/L NFZ for 24 hours. Results are shown as mean ± SD ($n = 3$ independent experiments with at least 10,000 cells counted in each replicate; ns, not significant; **, $P < 0.01$; ***, $P < 0.001$), compared with DMSO group by Dunnett multiple comparisons test.

We brought together the pathways affected by NFZ (**Fig. 2A**). In the NFZ groups, NFZ affected the function of several transcription factors (TF), including ERG in the MAPK signaling pathway (**Fig. 2A**), which directly led to the downregulation of cytokines IL1, IL6, and CCL2. Among the TFs, ELK1, and ETS1 belong to the ETS family because they have the same ETS domain (38). Studies have shown that ERG and other TFs containing ETS domains cooperate with multiple TFs (AP-1, NFAT, NFκB, etc.) or proteins to regulate downstream gene expression (39, 40). This implies that NFZ may affect the function of other TFs through interfering with ERG-related protein–protein interaction network.

In addition, it has been reported that cyclin D induces E2F-mediated progression to pass G1 and the R point, which can be inhibited by RB (41). Hossain and colleagues observed cell cycle arrest at G_1–G_0 by knocking down ERG (42). In the NFZ groups, we also observed that cyclin D was downregulated and RB was upregulated by NFZ through the MAPK signaling pathway, resulting in the failure of cells from the G_1–G_0 phase to the S phase (**Fig. 2A**). Cell-cycle experiments confirmed that the proportion of cells in the G_1–G_0 phase was increased with the increasing NFZ concentrations (**Fig. 2C**). Thus, NFZ can inhibit the proliferation of TMPRSS:ERG-positive cells by interfering with ERG or ERG-related TFs.

NFZ blocks the interaction between ERG and PARP1 and activates the parthanatos pathway

We also found NFZ upregulated DNA repair–related genes (including *BRCA1*, *FANCA*, and *PARP1*) in VCaP cells (**Fig. 2B**), especially PARP1. We tried to inhibit the DNA repair function through a PARP1 inhibitor (olaparib), so as to promote the killing effect of NFZ on tumor cells, but our statistics showed the opposite. Olaparib blocked NFZ-mediated growth inhibition on VCaP cells in a dose-dependent manner (**Fig. 3A**). A concentration of 20 μmol/L olaparib completely abrogated the inhibitory effects of NFZ. Therefore, we hypothesized that NFZ could block the binding of ERG and PARP1. We constructed a DU145 cell line, stably overexpressing a FLAG-tagged ERG, by lentiviral transfection (Supplementary Fig. S6). It was confirmed by coimmunoprecipitation that the 0.5 or 1 μmol/L NFZ reduced the amount of PARP1 bound to ERG (**Fig. 3B**). When we used PARP1 as bait protein, the amount of ERG also decreased by NFZ, whether by anti-PARP1 antibodies or magnetic beads pull-down of bait proteins (Supplementary Fig. S7). The reduction of PARP1 indicates that NFZ blocks the interaction between ERG and PARP1.

The inhibitory effect of NFZ requires PARP1 activity, which implicates an association with parthanatos. Parthanatos is different from other regulatory cell death pathways in that it depends on the activity of PARP1. So, NFZ may induce cell death by activating the parthanatos pathway (**Fig. 3C**). AIF is the main effector of parthanatos when nuclear translocation occurs, which will eventually produce a large number of DNA fragments to induce cell necrosis (43). RT-qPCR suggested that NFZ increased the expression of *AIF*, which was confirmed by RNA-seq (**Fig. 3D**; Supplementary Table), indicating that NFZ activated regulatory cell death pathways by increasing the expression of AIF. Western blotting also showed that NFZ rapidly released AIF at 2 or 5 μmol/L within 30 minutes, which was reduced by 10 μmol/L olaparib (**Fig. 3E**). Therefore, AIF induced by NFZ required the activity of PARP1. To verify whether NFZ results in DNA damage by parthanatos, we assessed the total levels of histone γ-H2A.X, which is rapidly phosphorylated in response to DNA double-stranded breaks (44). γ-H2A.X expression was increased by 2 or 5 μmol/L NFZ at different times (**Fig. 3F**), further supporting the activation of parthanatos. Olaparib also counteracted this effect of NFZ (**Fig. 3F**). These results imply the cell death function of NFZ requires the activation of PARP1.

We also assessed that the combination of olaparib and NFZ acted on the DU145-ERG cells. NFZ had a stronger inhibitory effect on the ERG overexpressing cell line (**Fig. 3G**). The difference in IC_{50} between DU145-ERG and DU145 vector is at least sevenfold (0.976 ± 0.131 vs. 7.68 ± 0.211 μmol/L, $p < 0.0001$), while the addition of olaparib reduces the inhibitory of NFZ on DU145-ERG at least 10-fold (**Fig. 3G**). These results indicate that the inhibitory effects of NFZ occur through ERG and need the participation of PARP1, which is characteristic of parthanatos activation.

NFZ also activates other regulatory cell death pathways

We observed that NFZ caused a large amount of DNA damage, which may induce the activation of other regulatory cell death pathways. Cleaved PARP1 can be produced by activated caspases, and is an important marker of apoptosis (45). NFZ increased PARP1 cleavage, but this effect was not altered by olaparib (**Fig. 4A**). This finding suggests that NFZ induces apoptosis separately from parthanatos.

At the same time, we visualized the target proteins (cleaved PARP1, AIF, and γ-H2A.X) by laser confocal imaging (**Fig. 4B** and **4C**). Cleaved PARP1 was increased by NFZ but had no obvious decrease in the olaparib and NFZ combination group compared with the NFZ group (**Fig. 4B**). The NFZ-induced cleaved PARP1 is mainly distributed in the cytoplasm, with a small amount in the nucleus (**Fig. 4B**). AIF is released from the mitochondria and functions in nucleus, so the increased AIF can be observed in the cytoplasm and nucleus of NFZ-treated cells (**Fig. 4B**). Laser confocal imaging for γ-H2A.X suggests that it is located in the nucleus and is upregulated by NFZ (**Fig. 4C**). Otherwise, the effect of NFZ on AIF and γ-H2A.X is counteracted by olaparib in the olaparib and NFZ combination group (**Fig. 4B** and **C**). These results are consistent with that of Western blotting.

PI strongly stains necrotic cells, while Hoechst staining could distinguish apoptotic cells from normal cells or necrotic cells (46). Flow cytometry analysis of PI and Hoechst staining suggests that the clusters of dead cells in 5, 10, or 20 μmol/L NFZ-treated cultures are grouped along the PI axis (Q1 and Q2), significantly higher than that in the DMSO group, which indicates that the dead cells are mainly necrotic cells related to the activation of parthanatos (**Fig. 4D**). In NFZ-treated cells, we also observed that the clusters of dead cells were grouped along Hoechst axes, indicating that the dead cells contained apoptotic cells (Q4; **Fig. 4D**). In the olaparib and NFZ combination group, olaparib reduced the number of necrotic cells (Q1 and Q2) significantly compared with NFZ-treated cells, but not the apoptotic cells (Q4). NFZ may activate different regulatory cell death pathways (parthanatos and apoptosis), while parthanatos is the principal cause of cell death.

Antitumor activity of NFZ *in vivo*

To test whether NFZ possesses antitumor activity on *TMPRSS:ERG*-positive cells *in vivo*, xenografts generated from VCaP cells were treated with vehicle or NFZ for 3 weeks. NFZ can reach a certain blood concentration by oral administration (47). An i.p. group was injected with 75 mg/kg NFZ once a day, while a gavage group was administered 37.5 mg/kg twice a day. As shown in **Fig. 5A**, VCaP cells responded to NFZ treatment, in both gavage

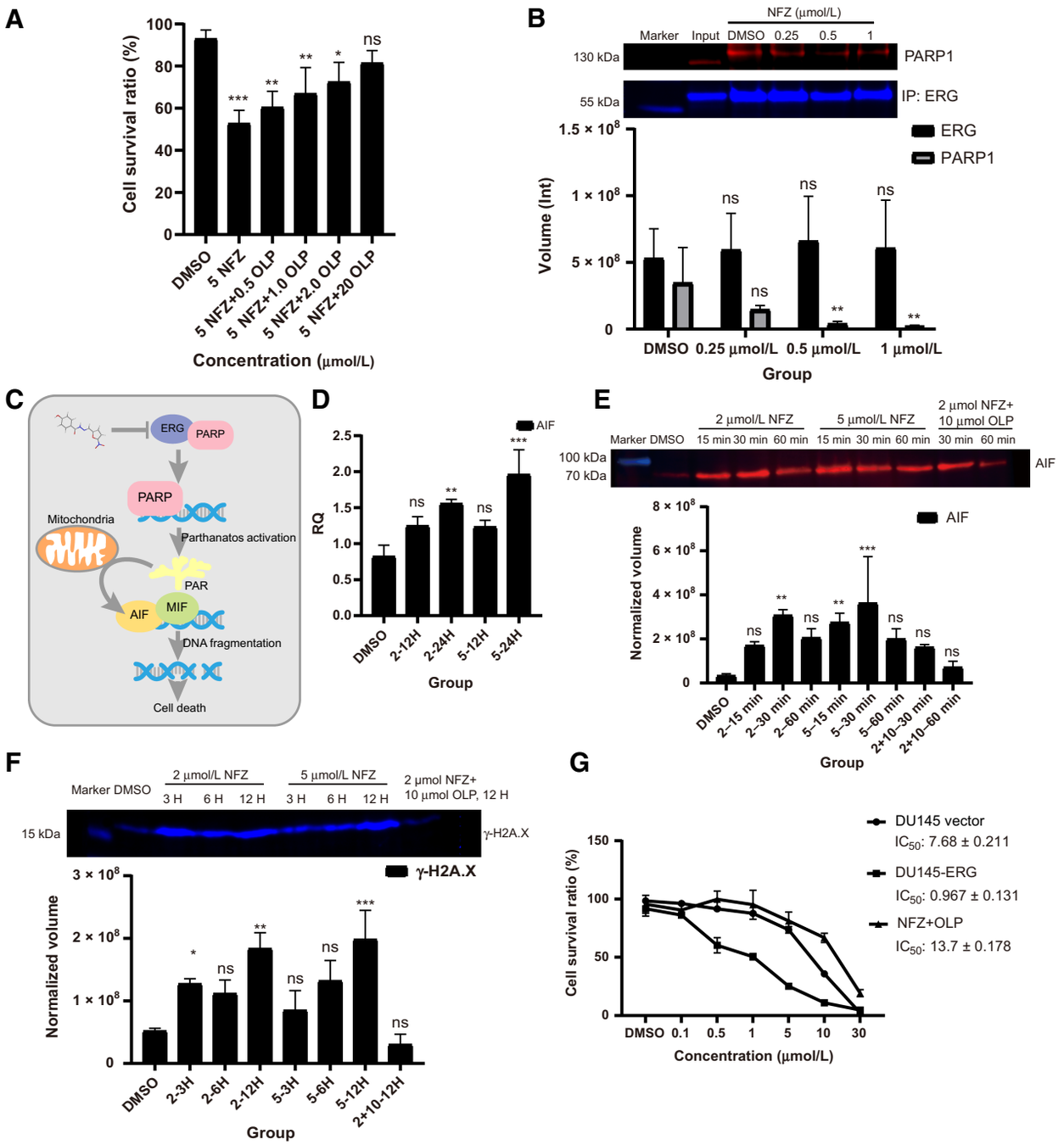

Figure 3.

NFZ activates parthanatos by blocking the interaction of ERG and PARP1. **A,** The combined effect of OLP and NFZ on VCaP cells. VCaP cells were treated with 5 μmol/L NFZ or 5 μmol/L NFZ combined with 0.5, 1.0, or 20 μmol/L OLP. The results in the histogram are shown as mean ± SD ($n = 3$ independent experiments; ns, not significant; *, $P < 0.05$; **, $P < 0.01$; ***, $P < 0.001$), compared with the DMSO group by Dunnett multiple comparisons test. **B,** Co-immunoprecipitation of ERG and PARP1 from ERG-overexpressing cells (DU145-ERG). Representative Western blotting is shown on top, and a quantitative histogram is shown beneath. Histogram results are shown as mean ± SD ($n = 5$ independent experiments; ns, not significant; *, $P < 0.05$; **, $P < 0.01$), compared with the DMSO group by Dunnett's multiple comparisons test. **C,** Illustration of parthanatos activated by NFZ. NFZ reduces the interaction of ERG and PARP1, so that overactive PARP1 activates the parthanatos pathway. **D,** RT-qPCR for AIF mRNA on VCaP cells. RQ, relative quantification. Abscissa indicates 2 or 5 μmol/L NFZ treatment for 12 or 24 hours. **E,** AIF Western blot. **F,** γ-H2A.X Western blotting. Representative Western blotting is shown on top, and a quantitative histogram is shown beneath it for the diagrams in E and F. VCaP cells were treated with DMSO, or 2, or 5 μmol/L NFZ, or NFZ combined with 10 μmol/L OLP for different times. Intensity was measured using Image lab 5.2 software and normalized to total protein. Relative expression is shown using the first sample as a reference. Uncropped blots are shown in Supplementary Figs. S6, 8S and 9S. Histogram results are shown as mean ± SD ($n = 3$ independent experiments; ns, not significant; *, $P < 0.05$;**, $P < 0.01$; ***, $P < 0.001$; ****, $P < 0.0001$), compared with the DMSO group by Dunnett multiple comparisons test. **G,** IC_{50} values for ERG-overexpressing cells. The DU145 vector group is the negative control group. The DU145-ERG group is the ERG-overexpressing group, which was treated with 0.1, 0.5, 1, 5, 10, and 30 μmol/L NFZ, or a mixture of the NFZ and 10 μmol/L OLP. IC_{50} values were obtained using GraphPad Prism 8.0. OLP, olaparib.

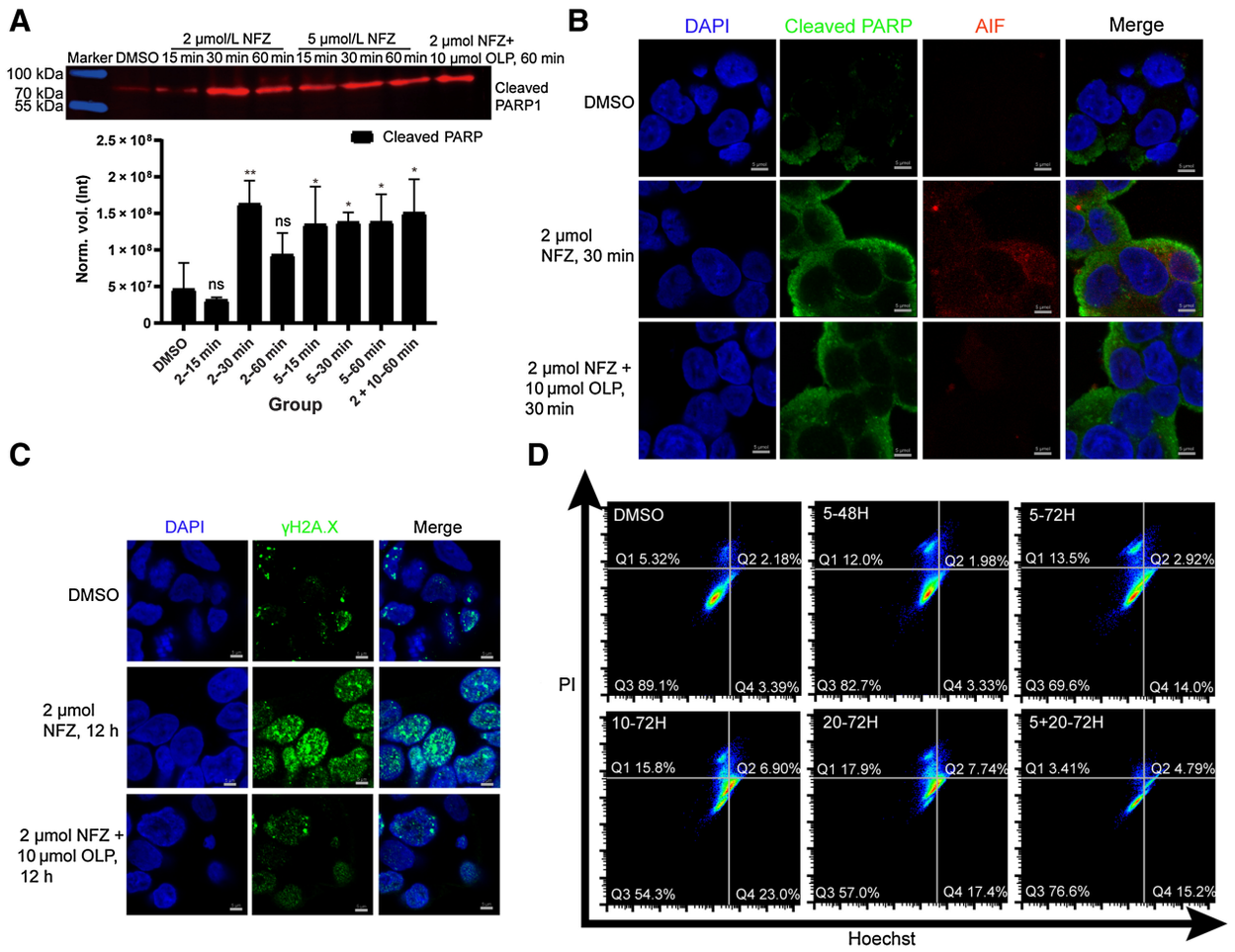

Figure 4.

NFZ induces apoptosis and necrosis. **A,** Western blotting for cleaved PARP1. Representative Western blot is shown on top and the quantitation is shown beneath. VCaP cells were treated with DMSO, or 2, or 5 μmol/L NFZ, or NFZ combined with 10 μmol/L OLP for different times. Band intensity was measured by Image Lab 5.2 software and normalized to total protein. Relative levels are expressed using the first sample as a reference. Uncropped blots are shown in Supplementary Fig. S10. Results in the histogram are shown as mean ± SD ($n = 3$ independent experiments; ns, not significant; *, $P < 0.05$;**, $P < 0.01$; ***, $P < 0.001$; ****, $P < 0.0001$), compared with the DMSO group by Dunnett multiple comparisons test. **B,** Confocal laser imaging for cleaved PARP1 and AIF. VCaP cells were treated with 2 μmol/L NFZ for 30 minutes. Immunofluorescence of cleaved PARP1 (green), AIF (red) and nuclei (DAPI, blue). Scale bars, 5 μm. **C,** Confocal laser imaging for γ-H2A.X. VCaP cells were treated with 2 μmol/L NFZ for 12 hours. Immunofluorescence of γ-H2A.X (green) and nuclei (DAPI, blue). Scale bars, 5 μm. **D,** Flow cytometry for cell death. Apoptotic cells and dead cells are stained by Hoechst to different degrees. VCaP cells were treated with 5 μmol/L NFZ, 10 μmol/L NFZ, or 20 μmol/L NFZ for 48 hours or 72 hours. Q1 and Q2 gate are the necrotic cells; Q3 and Q4 represent the normal cells and apoptotic cells, respectively. The results show the proportion of dead cells to the total number with at least 10,000 cells counted. DMSO was used as a control. OLP, olaparib.

and i.p. groups, with relative tumor volume compared with those in the control group. Both gavage and i.p. administration showed obvious tumor inhibitory activity by the third day (**Fig. 5A**). The antitumor activity of the i.p. group showing slightly better activity than the gavage group, suggesting that NFZ can exert antitumor activity by either oral administration or i.p. injection.

We further evaluated the effect of NFZ on the body weight of the mice. The weight loss of mice treated with NFZ was significantly less than that of mice treated with vehicle (**Fig. 5B**), implying that NFZ can reduce the weight loss of mice, and NFZ did not show obvious toxicity through our observation. The values of ALT and AST fluctuated within a normal range in the NFZ-treated groups (**Fig. 5C** and **D**; ref. 48). On the basis of the above data, NFZ could exert its antitumor function without obvious toxicity.

Discussion

To obtain a strong enough positive compound, we set the maximum IC_{50} value to 30 μmol/L. Andrographolide is derived from a natural product that needed structural modification for better pharmacokinetic characteristics due to its several unstable groups, whereas nifuratel has better activity and structure, indicating its structure would mediate a better structure-activity relationship. So, we focused our research on nitrofurans. NFZ inhibited the growth of the five cell lines to different extents, compared with napabucasin and disulfiram, which indicates NFZ's mode of action is different than napabucasin and disulfiram. SPR experiments showed that NFZ has affinity for STAT3 and ALDH1, but a stronger affinity for ERG. Because the double deduction system of Biacore and the speed of protein separation from the chip are different, the response value will fluctuate significantly

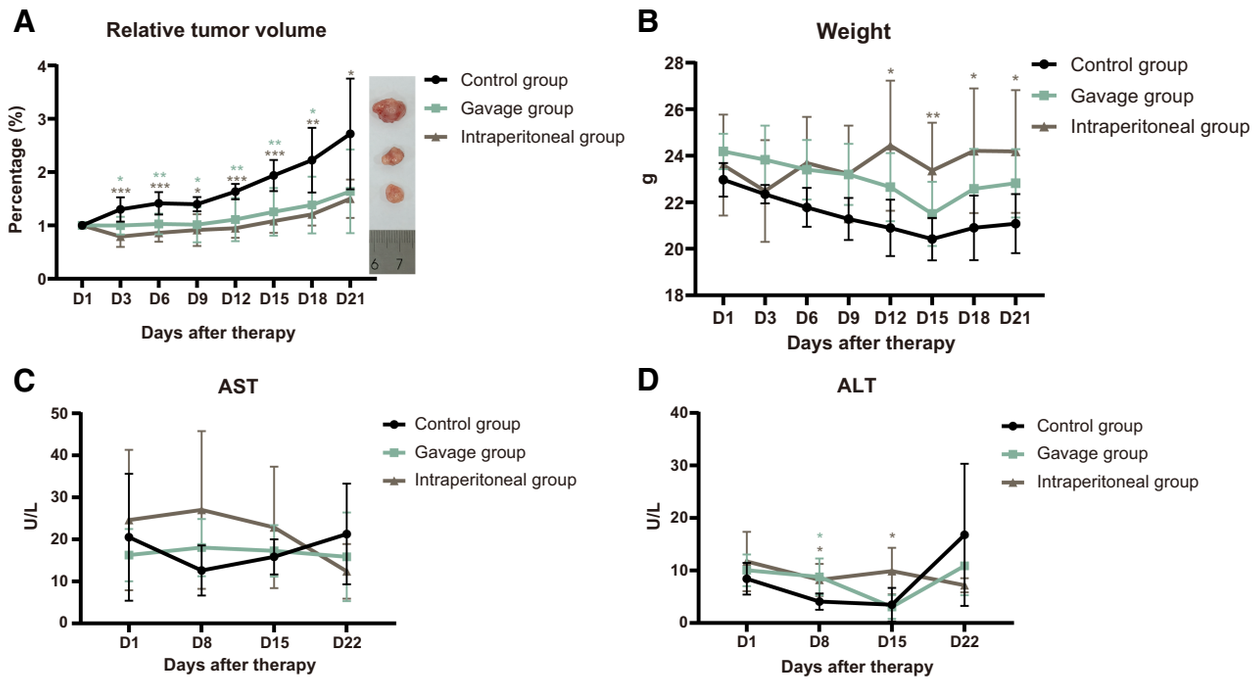

Figure 5.

Antitumor activity of NFZ *in vivo*. The treatment groups were injected i.p. with 75 mg/kg once a day or administered 37.5 mg/kg twice a day by gavage, while the control group was injected i.p. with the corresponding solvent. **A,** Visualized tumor tissues and the change of the relative tumor volume in different groups. **B,** Weight of the mice in different groups. **C,** Plasma AST levels in the different groups (**D**) Plasma ALT levels in the different groups. The results are shown as mean ± SD ($n = 6$; ns, not significant; *, $P < 0.05$;**, $P < 0.01$; ***, $P < 0.001$; ****, $P < 0.0001$), compared with the control group by Dunnett multiple comparisons test.

from low to high after deducting the solvent group (35, 36). This way will not change the binding mode between the receptor and ligand. NFZ shows an obvious strong inhibitory effect on the growth of ERG-positive cell lines (VCaP, DU145-ERG) but not ERG-negative cell lines (LNCaP, DU145, WPMY). NFZ is more likely to inhibit ERG to a greater extent when the three targets coexist. This would explain why nitrofurans also have a certain inhibitory effect on ERG-negative cell lines. At the same time, PC3 is a cell line with overexpression of ETV4 (a member of the ETS family), which is required for anchorage-independent growth and proliferation in PC3 prostate cells (49). NFZ showed a low IC_{50} on PC3 cells, indicating that NFZ could inhibit cell growth through different members of the ETS family.

PARP1 inhibition by olaparib can counteract the growth inhibitory effect of NFZ on VCaP cells, indicating NFZ-mediated cytotoxicity is exerted via PARP1, indicative of parthanatotic cell death. Coincidentally, Dinhof and colleagues also found that YK-4–279, mentioned above, can also activate the parthanatos through PARP1 (50). Overactivation of PARP1 is the key to parthanatos activation (43), which is likely related to NFZ blocking the interaction between ERG and PARP1 in our study. Li, G. Y. and colleagues elucidated that mTOR interacting with PARP1 could regulate parthanatos via the intermediate factor sirtuin 1 (51). Activating parthanatos by blocking the interaction between ERG and PARP1 is a new concept. Transcriptomics suggests that NFZ affects the function of downstream TFs in the MAPK signaling pathway, resulting in a reduction in expression of a large number of cytokines. Cell necrosis caused by NFZ activating parthanatos and the down-regulation of these inflammatory factors could change the immune microenvironment and improve the immune response. It has been reported that NFZ can increase the infiltration of $CD8^+$ T cells and reduce the number of M2 macrophages in colorectal cancer (52). This will be a new option in tumor treatment.

In vivo experiments indicate that NFZ shows antitumor activity at an early time point and could alleviate the weight loss of mice without obvious toxicity, either through gavage or i.p. administration. This will greatly accelerate drug compliance in future clinical applications. In many cancers, TFs are the most direct and promising targets, but the development of related inhibitors has seldom achieved results (53). "New use of old drugs" is a shortcut for the development of TF inhibitors. NFZ has a long history of clinical application, and there are many studies on its anticancer activity (54). However, now that it has been discovered for the first time that NFZ can target ETS-related proteins and can cause cell death by inducing excessive activation of PARP1, it is a potential that has yet to be explored. We hope to explore appropriate combination therapy to provide greater benefit for more patients.

Authors' Disclosures

C. Li reports a patent for "An inhibitor targeting ETS," licensed. A. Kumar reports other support from Li-Ka Shing Foundation during the conduct of the study. D.J. Kelvin reports a patent for "An inhibitor targeting ETS," licensed. No disclosures were reported by the other authors.

Authors' Contributions

C. Li: Conceptualization, data curation, software, formal analysis, validation, investigation, visualization, methodology, writing–original draft, project administration, writing–review and editing. **J. Zhang:** Data curation, validation, methodology.

Q. Wu: Data curation, visualization, methodology. **A. Kumar:** Software, formal analysis, methodology. **G. Pan:** Software, methodology. **D.J. Kelvin:** Resources, supervision, funding acquisition, methodology, writing–original draft, project administration, writing–review and editing.

Acknowledgments

The author thanks Professor Stanley L Lin for his suggestions on this paper. Financial support was provided by the Li-Ka Shing Foundation, Canadian Institutes for Health Research, and Research Nova Scotia (D.J. Kelvin). D.J. Kelvin is the recipient of the Canada Research Chair in Translational Vaccinology and Inflammation.

The publication costs of this article were defrayed in part by the payment of publication fees. Therefore, and solely to indicate this fact, this article is hereby marked "advertisement" in accordance with 18 USC section 1734.

Note

Supplementary data for this article are available at Molecular Cancer Therapeutics Online (http://mct.aacrjournals.org/).

Received March 5, 2022; revised August 24, 2022; accepted December 30, 2022; published first January 9, 2023.

References

1. Sung H, Ferlay J, Siegel RL, Laversanne M, Soerjomataram I, Jemal A, et al. Global cancer statistics 2020: GLOBOCAN estimates of incidence and mortality worldwide for 36 cancers in 185 countries. CA Cancer J Clin 2021;71:209–49.
2. Wang L, Paller CJ, Hong H, De Felice A, Alexander GC, Brawley O. Comparison of systemic treatments for metastatic castration-sensitive prostate cancer: a systematic review and network meta-analysis. JAMA Oncol 2021;7:412–20.
3. Vellky JE, Ricke WA. Development and prevalence of castration-resistant prostate cancer subtypes. Neoplasia 2020;22:566–75.
4. Flippot R, Patrikidou A, Aldea M, Colomba E, Lavaud P, Albigès L, et al. PARP inhibition, a new therapeutic avenue in patients with prostate cancer. Drugs 2022;82:719–33.
5. Mitsogiannis I, Tzelves L, Dellis A, Issa H, Papatsoris A, Moussa M. Prostate cancer immunotherapy. Expert Opin Biol Ther 2022;22:577–90.
6. Tomlins SA, Rhodes DR, Perner S, Dhanasekaran SM, Mehra R, Sun XW, et al. Recurrent fusion of TMPRSS2 and ETS transcription factor genes in prostate cancer. Science 2005;310:644–8.
7. Adamo P, Ladomery MR. The oncogene ERG: a key factor in prostate cancer. Oncogene 2016;35:403–14.
8. Mohamed AA, Xavier CP, Sukumar G, Tan SH, Ravindranath L, Seraj N, et al. Identification of a small molecule that selectively inhibits ERG-positive cancer cell growth. Cancer Res 2018;78:3659–71.
9. Eldhose B, Pandrala M, Xavier C, Mohamed AA, Srivastava S, Sunkara AD, et al. New selective inhibitors of ERG-positive prostate cancer: ERGi-USU-6 salt derivatives. ACS medicinal chemistry letters. 2021;12:1703–9.
10. Rahim S, Beauchamp EM, Kong Y, Brown ML, Toretsky JA, Uren A. YK-4–279 inhibits ERG and ETV1 mediated prostate cancer cell invasion. PLoS One 2011; 6:e19343.
11. Lamhamedi-Cherradi SE, Menegaz BA, Ramamoorthy V, Aiyer RA, Maywald RL, Buford AS, et al. An oral formulation of YK-4–279: preclinical efficacy and acquired resistance patterns in Ewing sarcoma. Mol Cancer Ther 2015;14:1591–604.
12. Carron MCE. Antibacterial nitrofurfuryldene derivatives and methods of using same. United States Patent Office 1966; US3290213. 1966.
13. Wishart DS, Feunang YD, Guo AC, Lo EJ, Marcu A, Grant JR, et al. DrugBank 5.0: a major update to the DrugBank database for 2018. Nucleic Acids Res 2018; 46:D1074–82.
14. Madej T, Lanczycki CJ, Zhang D, Thiessen PA, Geer RC, Marchler-Bauer A, et al. MMDB and VAST+: tracking structural similarities between macromolecular complexes. Nucleic Acids Res 2014;42:D297–303.
15. Shen C, Wang Z, Yao X, Li Y, Lei T, Wang E, et al. Comprehensive assessment of nine docking programs on type II kinase inhibitors: prediction accuracy of sampling power, scoring power and screening power. Brief Bioinform 2018.
16. O'Boyle NM, Banck M, James CA, Morley C, Vandermeersch T, Hutchison GR. Open babel: an open chemical toolbox. J Cheminform 2011;3:33.
17. Forli S, Huey R, Pique ME, Sanner MF, Goodsell DS, Olson AJ. Computational protein-ligand docking and virtual drug screening with the AutoDock suite. Nat Protoc 2016;11:905–19.
18. Regan MC, Horanyi PS, Pryor EE Jr, Sarver JL, Cafiso DS, Bushweller JH. Structural and dynamic studies of the transcription factor ERG reveal DNA binding is allosterically autoinhibited. Proc Natl Acad Sci USA. 2013;110: 13374–9.
19. Goodsell DS, Morris GM, Olson AJ. Automated docking of flexible ligands: applications of AutoDock. J Mol Recognit 1996;9:1–5.
20. Brown J, Pirrung M, McCue LA. FQC dashboard: integrates FastQC results into a web-based, interactive, and extensible FASTQ quality control tool. Bioinformatics 2017;33:3137–9.
21. Bolger AM, Lohse M, Usadel B. Trimmomatic: a flexible trimmer for Illumina sequence data. Bioinformatics 2014;30:2114–20.
22. Dobin A, Davis CA, Schlesinger F, Drenkow J, Zaleski C, Jha S, et al. STAR: ultrafast universal RNA-seq aligner. Bioinformatics 2013;29:15–21.
23. Brenner J, Ateeq B, Li Y, Yocum A, Cao Q, Asangani I, et al. Mechanistic rationale for inhibition of poly(ADP-ribose) polymerase in ETS gene fusion-positive prostate cancer. Cancer Cell 2011;19:664–78.
24. Eaton SL, Roche SL, Llavero Hurtado M, Oldknow KJ, Farquharson C, Gillingwater TH, et al. Total protein analysis as a reliable loading control for quantitative fluorescent Western blotting. PLoS One 2013;8:e72457.
25. Korenchuk S, Lehr JE, MClean L, Lee YG, Whitney S, Vessella R, Lin DL, et al. VCaP, a cell-based model system of human prostate cancer. In Vivo 2001;15: 163–8.
26. Gibas Z, Becher R, Kawinski E, Horoszewicz J, Sandberg AA. A high-resolution study of chromosome changes in a human prostatic carcinoma cell line (LNCaP). Cancer Genet Cytogenet 1984;11:399–404.
27. Stone KR, Mickey DD, Wunderli H, Mickey GH, Paulson DF. Isolation of a human prostate carcinoma cell line (DU 145). Int J Cancer 1978;21: 274–81.
28. Kaighn ME, Narayan KS, Ohnuki Y, Lechner JF, Jones LW. Establishment and characterization of a human prostatic carcinoma cell line (PC-3). Invest Urol 1979;17:16–23.
29. Bello D, Webber MM, Kleinman HK, Wartinger DD, Rhim JS. Androgen responsive adult human prostatic epithelial cell lines immortalized by human papillomavirus 18. Carcinogenesis 1997;18:1215–23.
30. Nelson EA, Walker SR, Kepich A, Gashin LB, Hideshima T, Ikeda H, et al. Nifuroxazide inhibits survival of multiple myeloma cells by directly inhibiting STAT3. Blood 2008;112:5095–102.
31. Sarvi S, Crispin R, Lu Y, Zeng L, Hurley TD, Houston DR, et al. ALDH1 bioactivates nifuroxazide to eradicate ALDH(High) melanoma-initiating cells. Cell Chem Biol 2018;25:1456–69.
32. Jin N, Zhu X, Cheng F, Zhang L. Disulfiram/copper targets stem cell-like ALDH (+) population of multiple myeloma by inhibition of ALDH1A1 and hedgehog pathway. J Cell Biochem 2018;119:6882–93.
33. Han D, Yu T, Dong N, Wang B, Sun F, Jiang D. Napabucasin, a novel STAT3 inhibitor suppresses proliferation, invasion and stemness of glioblastoma cells. J Exp Clin Cancer Res 2019;38:289.
34. Taylor SC, Posch A. The design of a quantitative Western blot experiment. Biomed Res Int 2014;2014:361590.
35. Haseley SR, Vermeer HJ, Kamerling JP, Vliegenthart JF. Carbohydrate self-recognition mediates marine sponge cellular adhesion. Proc Natl Acad Sci USA 2001;98:9419–24.
36. Si L, Meng K, Tian Z, Sun J, Li H, Zhang Z, et al. Triterpenoids manipulate a broad range of virus-host fusion via wrapping the HR2 domain prevalent in viral envelopes. Sci Adv 2018;4:eaau8408.
37. Tomlins SA, Laxman B, Varambally S, Cao X, Yu J, Helgeson BE, et al. Role of the TMPRSS2-ERG gene fusion in prostate cancer. Neoplasia 2008;10:177–88.
38. Sizemore GM, Pitarresi JR, Balakrishnan S, Ostrowski MC. The ETS family of oncogenic transcription factors in solid tumors. Nat Rev Cancer 2017;17:337–51.
39. Verger A, Buisine E, Carrère S, Wintjens R, Flourens A, Coll J, et al. Identification of amino acid residues in the ETS transcription factor Erg that mediate Erg-Jun/Fos-DNA ternary complex formation. J Biol Chem 2001;276:17181–9.
40. Bassuk AG, Anandappa RT, Leiden JM. Physical interactions between Ets and NF-kappaB/NFAT proteins play an important role in their cooperative activation of the human immunodeficiency virus enhancer in T cells. J Virol 1997;71: 3563–73.

41. Cobrinik D. Pocket proteins and cell-cycle control. Oncogene 2005;24:2796–809.
42. Hossain D, Bostwick DG. Significance of the TMPRSS2:ERG gene fusion in prostate cancer. BJU Int 2013;111:834–5.
43. Wang Y, An R, Umanah GK, Park H, Nambiar K, Eacker SM, et al. A nuclease that mediates cell death induced by DNA damage and poly(ADP-ribose) polymerase-1. Science 2016;354.
44. Ismail IH, Hendzel MJ. The gamma-H2A.X: is it just a surrogate marker of double-strand breaks or much more? Environ Mol Mutagen 2008;49: 73–82.
45. Genin M, Clement F, Fattaccioli A, Raes M, Michiels C. M1 and M2 macrophages derived from THP-1 cells differentially modulate the response of cancer cells to etoposide. BMC Cancer 2015;15:577.
46. Crowley LC, Marfell BJ, Waterhouse NJ. Analyzing cell death by nuclear staining with Hoechst 33342. Cold Spring Harb Protoc 2016;2016.
47. Labaune JP, Moreau JP, Byrne R. Comparative physiological disposition of two nitrofuran anti-microbial agents. Biopharm Drug Dispos 1986;7:431–41.
48. Mazzaccara C, Labruna G, Cito G, Scarfò M, De Felice M, Pastore L, et al. Age-related reference intervals of the main biochemical and hematological parameters in C57BL/6J, 129SV/EV, and C3H/HeJ mouse strains. PLoS One 2008;3:e3772.
49. Hollenhorst PC, Paul L, Ferris MW, Graves BJ. The ETS gene ETV4 is required for anchorage-independent growth and a cell proliferation gene expression program in PC3 prostate cells. Genes Cancer 2011;1:1044–52.
50. Dinhof C, Pirker C, Kroiss P, Kirchhofer D, Gabler L, Gojo J, et al. p53 loss mediates hypersensitivity to ETS transcription factor inhibition based on PARylation-mediated cell death induction. Cancers 2020;12:3205.
51. Pan YR, Song JY, Fan B, Wang Y, Che L, Zhang SM, et al. mTOR may interact with PARP1 to regulate visible light-induced parthanatos in photoreceptors. Cell Commun Signal 2020;18:27.
52. Ye TH, Yang FF, Zhu YX, Li YL, Lei Q, Song XJ, et al. Inhibition of Stat3 signaling pathway by nifuroxazide improves antitumor immunity and impairs colorectal carcinoma metastasis. Cell Death Dis 2017;8:e2534.
53. Darnell JE Jr. Transcription factors as targets for cancer therapy. Nat Rev Cancer 2002;2:740–9.
54. Bailly C. Toward a repositioning of the antibacterial drug nifuroxazide for cancer treatment. Drug Discov Today 2019;24:1930–6.